

Entanglement spectrum and boundary theories with projected entangled-pair statesJ. Ignacio Cirac,¹ Didier Poilblanc,² Norbert Schuch,³ and Frank Verstraete⁴¹Max-Planck-Institut für Quantenoptik, Hans-Kopfermann-Str. 1, D-85748 Garching, Germany²Laboratoire de Physique Théorique, CNRS and Université de Toulouse, F-31062 Toulouse, France³Institute for Quantum Information, California Institute of Technology, MC 305-16, Pasadena, California 91125, USA⁴Vienna Center for Quantum Technologies, Faculty of Physics, University of Vienna, A-1090 Vienna, Austria

(Received 21 March 2011; revised manuscript received 21 April 2011; published 29 June 2011)

In many physical scenarios, close relations between the bulk properties of quantum systems and theories associated with their boundaries have been observed. In this work, we provide an exact duality mapping between the bulk of a quantum spin system and its boundary using projected entangled-pair states. This duality associates to every region a Hamiltonian on its boundary, in such a way that the entanglement spectrum of the bulk corresponds to the excitation spectrum of the boundary Hamiltonian. We study various specific models: a deformed AKLT model [I. Affleck, T. Kennedy, E. H. Lieb, and H. Tasaki, *Phys. Rev. Lett.* **59**, 799 (1987)], an Ising-type model [F. Verstraete, M. M. Wolf, D. Perez-Garcia, and J. I. Cirac, *Phys. Rev. Lett.* **96**, 220601 (2006)], and Kitaev's toric code [A. Kitaev, *Ann. Phys.* **303**, 2 (2003)], both in finite ladders and in infinite square lattices. In the second case, some of those models display quantum phase transitions. We find that a gapped bulk phase with local order corresponds to a boundary Hamiltonian with local interactions, whereas critical behavior in the bulk is reflected on a diverging interaction length of the boundary Hamiltonian. Furthermore, topologically ordered states yield nonlocal Hamiltonians. Because our duality also associates a boundary operator to any operator in the bulk, it in fact provides a full holographic framework for the study of quantum many-body systems via their boundary.

DOI: [10.1103/PhysRevB.83.245134](https://doi.org/10.1103/PhysRevB.83.245134)

PACS number(s): 71.10.-w, 03.67.-a, 02.70.-c

I. INTRODUCTION

It has long been speculated that the boundary plays a very significant role in establishing the physical properties of a quantum field theory. This idea has been very fruitful in clarifying the physics of the fractional quantum Hall effect, and it is also the origin of the holographic principle in black hole physics. An explicit manifestation of this fact is the so-called area law. The area law states that for ground (thermal) states of lattice systems with short-range interactions, the entropy (quantum mutual information) of the reduced density operator ρ_A , corresponding to a region A , is proportional to the surface of that region rather than to the volume, at least for gapped systems.¹⁻⁴ Criticality may reflect itself in the appearance of multiplicative and/or linear logarithmic corrections to the area law.^{5,6}

Apart from the deep physical significance of this law, it has important implications regarding the possibility of simulating many-body quantum systems using tensor network (TN) states.⁷⁻¹⁰ For instance, it has been shown¹¹ that any state of a quantum spin system fulfilling the area law in one spatial dimension (including logarithmic violations) can be efficiently represented by a matrix product state (MPS),^{12,13} the simplest version of a TN.

Very recently, another remarkable discovery has been made with relation to the area law.¹⁴ It has been shown that for certain models in two spatial dimensions the reduced density matrix of a region A has a very peculiar spectrum, which is called the entanglement spectrum: by taking the logarithm of the eigenvalues of ρ_A , one obtains a spectrum that resembles very much that of a one-dimensional critical theory (i.e., as prescribed by conformal field theory). This has been established for different systems as diverse as gapped fractional quantum Hall states¹⁴ or spin-1/2 quantum

magnets.¹⁵ Interestingly, the correlation length in the bulk of the ground state can be naturally interpreted as a thermal length in one dimension.¹⁵

This is all very suggestive of the fact that the reduced density matrix is the thermal state of a one-dimensional theory. However, there is a clear mismatch in dimensions: the Hilbert space associated to ρ_A has two spatial dimensions, whereas the one-dimensional theory obviously has only one. Intuitively, this is clear because all relevant degrees of freedom of ρ_A should be located around the boundary of region A . The main question addressed in this paper is to explicitly identify the degrees of freedom on which this one-dimensional Hamiltonian acts.

We show that projected entangled-pair states (PEPS)¹⁶ give a very natural answer to that question. The degrees of freedom of the one-dimensional theory correspond to the virtual particles which appear in the valence bond description of PEPS and that “live” at the boundary of region A .^{16,17} More specifically, PEPS are built by considering a set of virtual particles at each node of the lattice, which are then projected out to obtain the state of the physical spins. As we show, the boundary Hamiltonian can be thought of as acting on the virtual particles that live at the boundary of region A . Furthermore, we present evidence that, for gapped systems, such a boundary Hamiltonian is quasilocal (i.e., it contains only short-range interactions) in terms of those (localized) virtual particles. As a quantum phase transition is approached, the range of the interactions increases. Finally, we show that the interactions lose their local character for the case of quantum systems exhibiting topological order. We also show how operators in the bulk can be mapped to operators on the boundary.

The fact that the boundary Hamiltonian is quasilocal has important implications for the theory of PEPS which

go well beyond those of the area law. While PEPS are expected to accurately represent the low-energy sector of local Hamiltonians in arbitrary dimensions,¹⁸ it has not been proven that one can use them to determine expectation values in an efficient and accurate way. For that, one has to contract a set of tensors, a task which could in principle require exponential time in the size of the lattice. In order to circumvent this problem, a method was introduced¹⁶ which successively approximates the boundary of a growing region by a matrix product density operator, which is exactly the density matrix of local virtual particles discussed before. It is not clear *a priori* to which extent that density matrix can be approximated by a MPS; more specifically, the bond dimension of that MPS could in principle grow exponentially with the size of the system if a prescribed accuracy is to be reached, which would lead to an exponential scaling of the computational effort. However, that MPS does nothing but approximate the boundary density operator ρ_A for different regions A . In case such an operator can be written as a thermal state of a quasilocal Hamiltonian, it immediately follows that in order to approximate it by a MPS one just needs a bond dimension that scales polynomially with the lattice size,¹⁸ and thus the expectation values of PEPS can be efficiently determined.

II. PEPS AND BOUNDARY THEORIES

A. Model

We consider a PEPS, $|\Psi\rangle$, of an $N_v \times N_h$ spin lattice in two spatial dimensions. Note that one can always find a finite-range interaction Hamiltonian for which $|\Psi\rangle$ is a ground state.¹⁹ We assume that we have open (periodic) boundary conditions in the horizontal (vertical) direction: the spins are regularly placed on a cylinder and the state $|\Psi\rangle$ is translationally invariant along the vertical direction (see Fig. 1). All spins have total spin S , except perhaps at the boundaries where we may choose a different spin in order to lift degeneracies related to the open boundary conditions. We are interested in the reduced density operator, ρ_ℓ , corresponding to the spins lying in the first ℓ columns, that is, when we trace all the spins from column $\ell + 1$ to N_h .

More specifically, the effective Hamiltonian H_ℓ , corresponding to those spins, is defined through $\rho_\ell = \exp(-H_\ell)/Z_\ell$, with Z_ℓ a normalization constant. We are interested not only in the entanglement spectrum¹⁴ but also in the specific form of H_ℓ and its interaction length, as we define below.

In order to simplify the notation, it is convenient to label the spin indices of each column with a single vector. We define $I_n = (i_{1,n}, i_{2,n}, \dots, i_{N_v,n})$, where $i_{k,n} = -S, -S + 1, \dots, S$ for $n = 2, \dots, N_h - 1$. (For $n = 1$ or $n = N_h$ we may have different spin S .) Thus, we can write

$$|\Psi\rangle = \sum_I c_I |I_1, I_2, \dots, I_{N_h}\rangle. \quad (1)$$

For a PEPS we can write

$$c_I = \sum_{\Lambda} L_{\Lambda_1}^{I_1} B_{\Lambda_1, \Lambda_2}^{I_2} \dots B_{\Lambda_{N_h-2}, \Lambda_{N_h-1}}^{I_{N_h-1}} R_{\Lambda_{N_h-1}}^{I_{N_h}}. \quad (2)$$

Here $\Lambda_n = (\alpha_{1,n}, \alpha_{2,n}, \dots, \alpha_{N_v,n})$, where $\alpha_{k,n} = 1, 2, \dots, D$ and D is the so-called bond dimension. Each of the B^I 's can be expressed in terms of a single tensor, \hat{A}^i ,

$$B_{\Lambda_{n-1}, \Lambda_n}^{I_n} = \text{tr} \left[\prod_{k=1}^{N_v} \hat{A}_{\alpha_{k,n-1}, \alpha_{k,n}}^{i_{k,n}} \right], \quad (3)$$

where for each value of i, α, α' , $\hat{A}_{\alpha, \alpha'}^i$ is a $D \times D$ matrix, with elements $A_{\alpha, \alpha'; \beta, \beta'}^i$ (where the indices α and β correspond to the virtual particles entangled along the horizontal and vertical directions, respectively;¹⁶ see Fig. 1). For the first (left) and last (right) column we define L^I and R^I similarly in terms of the $D \times D$ matrices \hat{l}_α^i and $\hat{r}_{\alpha'}^i$:

$$L_{\Lambda_1}^{I_1} = \text{tr} \left[\prod_{k=1}^{N_v} \hat{l}_{\alpha_{k,1}}^{i_{k,1}} \right], \quad (4)$$

$$R_{\Lambda_{N_h-1}}^{I_{N_h}} = \text{tr} \left[\prod_{k=1}^{N_v} \hat{r}_{\alpha_{k,N_h-1}}^{i_{k,N_h}} \right]. \quad (5)$$

Thus, the tensors \hat{A} , \hat{l} , and \hat{r} (for which explicit expressions are given later) completely characterize the state $|\Psi\rangle$, which is obtained by ‘‘tiling’’ them on the surface of the cylinder. The first has rank 5, whereas the other two have rank 4. Here we have taken all the tensors A to be equal, but they can be chosen to be different if the appropriate symmetries are not present.

B. Boundary density operator

We now want to express the reduced density operator ρ_ℓ in terms of the original tensors. In order to do that, we block all

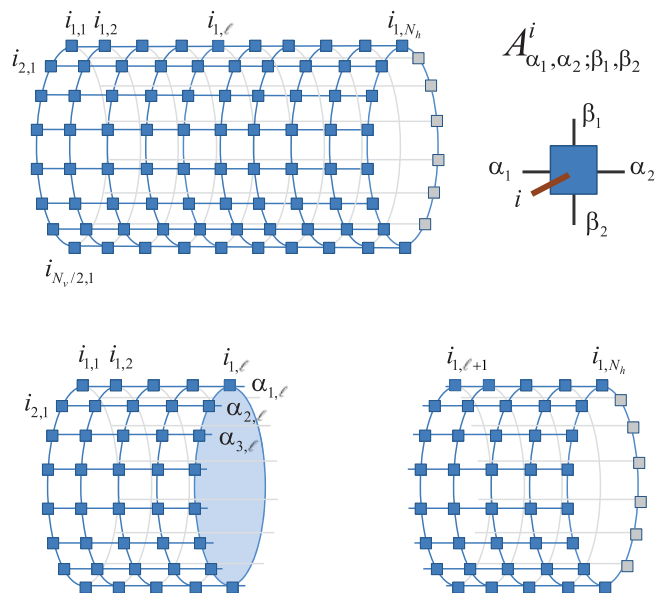


FIG. 1. (Color online) (top) We consider an $N_v \times N_h$ spin lattice in a cylindrical geometry. The PEPS is obtained by replacing each lattice site with a tensor A and contracting the virtual indices α and β along the horizontal and vertical directions. (bottom) We cut the lattice into two pieces, left and right. The virtual indices α of the tensors A along the cut are shown. The state $|\Psi_L\rangle$ acts on the spins $(i_{k,n})$ as well as on the virtual spins along the cut.

the spins that are in the first ℓ columns, and those in the last $N_h - \ell$ columns, and define

$$\hat{L}^{I_a} = L^{I_1} B^{I_2} \dots B^{I_\ell}, \quad \hat{R}^{I_b} = B^{I_{\ell+1}} \dots B^{I_{N_h-1}} R^{I_{N_h}}, \quad (6)$$

where we have collected all the indices I_1, \dots, I_ℓ in I_a and the rest in I_b . With this notation, the state $|\Psi\rangle$ can be considered a two-leg ladder, i.e., $\hat{N}_h = 2$, and $\hat{\ell} = 1$, where ρ_ℓ is the density operator corresponding to a single leg. Thus, we have

$$|\Psi\rangle = \sum_{I_a, I_b} \sum_{\Lambda} \hat{L}_{\Lambda}^{I_a} \hat{R}_{\Lambda}^{I_b} |I_a, I_b\rangle. \quad (7)$$

It is convenient to consider the space where the vectors L^I and R^I act as a Hilbert space and to use the bra-ket notation there as well. That space, which we call *virtual space*, is the one corresponding to the ancillas that build the PEPS in the valence bond construction.¹⁶ They are associated to the boundary between the ℓ th and the $(\ell + 1)$ st columns of the original spins. The dimension is thus D^{N_v} (see Fig. 1). In order to avoid confusion with the space of the spins, we have used $|v\rangle$ to denote vectors on that space. We can define the (unnormalized) joint state for the first ℓ columns and the virtual space, $|\Psi_L\rangle$, and similarly for the last columns, $|\Psi_R\rangle$, as

$$|\Psi_L\rangle = \sum_{I_a} |\hat{L}^{I_a}\rangle |I_a\rangle, \quad |\Psi_R\rangle = \sum_{I_b} |\hat{R}^{I_b}\rangle |I_b\rangle \quad (8)$$

with

$$|\hat{L}^{I_a}\rangle = \sum_{\Lambda} \hat{L}_{\Lambda}^{I_a} |\Lambda\rangle, \quad |\hat{R}^{I_b}\rangle = \sum_{\Lambda} \hat{R}_{\Lambda}^{I_b} |\Lambda\rangle, \quad (9)$$

and $|\Lambda\rangle$ the canonical orthonormal basis in the corresponding virtual spaces. The state $|\Psi\rangle$ can then be straightforwardly defined in terms of those two states. The corresponding reduced density operators for both virtual spaces are

$$\sigma_L = \sum_{I_a} |\hat{L}^{I_a}\rangle \langle \hat{L}^{I_a}|, \quad \sigma_R = \sum_{I_b} |\hat{R}^{I_b}\rangle \langle \hat{R}^{I_b}|. \quad (10)$$

In terms of these operators, it is very simple to show that

$$\rho_\ell = \sum_{\Gamma, \Gamma'} |\chi_\Gamma\rangle \langle \chi_{\Gamma'}| (\Gamma | \sqrt{\sigma_L^T} \sigma_R \sqrt{\sigma_L^T} | \Gamma'), \quad (11)$$

where $|\Gamma\rangle$ is an orthonormal basis of the range of σ_L , σ_L^T is the transpose of σ_L in the basis $|\Lambda\rangle$, and we have defined an orthonormal set (in the spin space)

$$|\chi_\Gamma\rangle = \sum_I (\Gamma | \frac{1}{\sqrt{\sigma_L}} | \hat{L}^I \rangle | I). \quad (12)$$

Now, defining an isometric operator that transforms the virtual onto the spin space $\mathcal{U} = \sum_{\Gamma} |\chi_\Gamma\rangle \langle \Gamma|$, we have

$$\rho_\ell = U \sqrt{\sigma_L^T} \sigma_R \sqrt{\sigma_L^T} U^\dagger. \quad (13)$$

The isometry U can also be used to map any operator acting on the bulk onto the virtual spin space. Note that this map is an isometry and hence not injective; i.e., a boundary operator might correspond to many different bulk operators. This is of course a necessity, as U is responsible for mapping a two-dimensional theory to a one-dimensional one.

C. Boundary Hamiltonian

The previous equation shows that ρ_ℓ is directly related to the density operators corresponding to the virtual space of the ancillary spins that build the PEPS. In particular, if we have $\sigma_L^T = \sigma_R =: \sigma_b$ (e.g., when we have the appropriate symmetries as in the specific cases analyzed below), then $\rho_\ell = U \sigma_b^2 U^\dagger$. The reduced density operator ρ_ℓ is thus directly related to that of the virtual spins along the boundary. Since U is isometric it conserves the spectrum and thus the entanglement spectrum of ρ_ℓ coincides with that of σ_b^2 . By writing $\sigma_b^2 = \exp(-H_b)$, we obtain an effective one-dimensional Hamiltonian for the virtual spins at the boundary of the two regions whose spectrum coincides with the entanglement spectrum of ρ_ℓ .

We are interested to see to what extent H_b is a local Hamiltonian for the boundary (virtual) space. We can always write H_b as a sum of terms involving different spin operators. For instance, for $D = 2$, we can take the Pauli operators σ_α ($\alpha = x, y, z$) acting on different spins, and the identity operator on the rest. We group those terms into sums h_n , where each h_n contains all terms with interaction range n , i.e., for which the longest contiguous block of identity operators has length $N_v - n$. For instance, h_0 contains only one term, which is a constant; h_1 contains all terms where only one Pauli operator appears; and h_{N_v} contains all terms where no identity operator appears. We define

$$d_n = \text{tr}(h_n^2) / 2^{N_v}, \quad (14)$$

which expresses the strength of all the terms in the Hamiltonian with interaction length equal to n . A fast decrease of d_n with n indicates that the effective Hamiltonian describing the virtual boundary is quasilocal. In the examples we examine below, this is the case as long as we do not have a quantum phase transition. In such a case, the length of the effective Hamiltonian interaction increases.

D. Implications for PEPS

In the case σ_b can be written in terms of a local boundary Hamiltonian, one can draw important consequences for the theory of PEPS. In particular, it implies that the PEPS can be efficiently contracted, and correlation functions can be efficiently determined. The reason can be understood as follows. Let us consider again the cylindrical geometry (Fig. 1), and let us assume that we want to determine any correlation function along the vertical direction, e.g., at the lattice points $(\ell, 1)$ and (ℓ, x) . It is very easy to show that such a quantity can be expressed in terms of σ_L and σ_R . If we are able to write these two operators as matrix product operators (MPOs), i.e., as

$$\sum_{i_n, j_n, =1}^D \text{tr}[M^{i_1, j_1} \dots M^{i_{N_v}, j_{N_v}}] |i_1, \dots, i_{N_v}\rangle \langle j_1, \dots, j_{N_v}|, \quad (15)$$

where the M are $D' \times D'$ matrices, then the correlation function can be determined with an effort that scales as $N_v (D')^6$. It was shown by Hastings¹⁸ that if an operator can be written as $\exp(-H_b/2)$, where H_b is quasilocal, then it can be efficiently represented by a MPO; that is, the bond dimension D' only scales polynomially with N_v . Thus, the time required

to determine correlation functions only scales polynomially with N_v .

Later, when we examine various examples, we use a MPO to represent σ_b . In that case, we can directly check if we obtain a good approximation by using a MPO by simply observing how much errors increase when we decrease the bond dimension D' . We see that the error increases when we approach a quantum phase transition. Furthermore, whenever σ_b can be well approximated by a MPO, we can use the knowledge gained in the context of MPS^{12,13} to observe the appearance of a quantum phase transition in the original PEPS. For that, we just have to recall that the correlation length ξ is related to the two largest (in magnitude) eigenvalues, $\lambda_{1,2}$, of the matrix $\sum_i M^{i,i}$; $\xi = 1/\ln(|\lambda_1/\lambda_2|)$. For $|\lambda_1| = |\lambda_2|$, the correlation length diverges, indicating the presence of a quantum phase transition.

E. Qualitative discussion

In order to better understand the structure of σ_b , let us first consider a one-dimensional (1D) spin chain. Even though the boundary of the chain, when cut into two parts, has zero dimensions, it helps us to understand the two-dimensional (2D) systems. We take $N_v = 1$ so that the PEPS reduces to a MPS. We can use the theory of MPS^{12,13} to analyze the properties of the completely positive map (CPM) \mathcal{E} . (The matrices A^i of the MPS are the Kraus operators of the CPM.) In the limit $N_h \rightarrow \infty$, σ_b is nothing but the fixed point of such a CPM. For gapped systems, \mathcal{E} has a unique fixed point, and thus σ_b is unique. For gapless systems, \mathcal{E} becomes block diagonal (and thus there are several fixed points), the correlation length diverges, and we can write

$$\sigma_b = \bigoplus_{n=1}^B p_n \sigma_b^{(n)}, \quad (16)$$

where B is the number of blocks which coincides with the degeneracy of the eigenvalue of \mathcal{E} corresponding to the maximum magnitude. In such a case, the weights p_n depend on the tensors l and r which are chosen at the boundaries. For critical systems, one typically finds that D increases as a polynomial in N_v such that one obtains logarithmic corrections to the area law.^{6,20}

The 2D geometry considered here reduces to the 1D case if we take the limit $N_h \rightarrow \infty$ by keeping N_v finite. According to the discussion above, we expect to have a unique σ_b if we deal with a gapped system. As we illustrate below with some specific examples, this operator can be written in terms of a local Hamiltonian H_b of the boundary virtual space which is quasilocal. As we approach a phase transition, the gap closes and the correlation length diverges. In some cases, the boundary density operator can be written as a direct sum (16), eventually leading to the loss of locality in the boundary Hamiltonian.

III. NUMERICAL METHODS

In order to determine σ_b we make heavy use of the fact that $|\Psi\rangle$ is a PEPS. We have followed three different complementary numerical approaches that we briefly describe here.

A. Iterative procedure

First of all, for sufficiently small values of N_v (typically $N_v \leq 12$), we can perform exact numerical calculations and determine $\sigma_{L,R}$ according to Eq. (10). The main idea is to start from the left and find first σ_L for $\ell = 1$ by contracting the tensors l^i appropriately. Then, we can proceed for $\ell = 2$ by contracting the tensors A^i corresponding to the second column. In this vein, and as long as N_v is sufficiently small, we can determine $\sigma_{L,R}$ for all values of ℓ and N_h .

B. Exact contractions and finite size scaling

The second (exact) method is a variant applicable to larger values of N_v (typically up to $N_v = 20$) but restricted to a finite width in the horizontal direction. It consists of exactly contracting the internal indices of two adjacent blocks of size $N_v/2 \times N_h$. These two blocks are then contracted together in a second step. Although limited by the size $2^{N_v+2N_h}$ of the half block (which has to fit in the computer RAM), this approach can still handle systems of size 20×2 or 16×8 and can be supplemented by a finite size scaling analysis.

C. Truncation method

Finally, to take the $N_h \rightarrow \infty$ limit, we can use the methods introduced in Ref. 16 to approximate the column operators. The main idea is to represent those operators by tensor networks with the structure of a MPS. We contract one column after another, finding the optimal MPS after each contraction variationally. In particular, since we consider translationally invariant states, we can choose the matrices of the corresponding MPS to all be equal, which simplifies the procedure. We can even approach the limit $N_v, N_h \rightarrow \infty$ as follows (see also Refs. 9 and 21):

- (i) We start out with $\ell = 1$ and contract the second column, obtaining another tensor network with the same MPS structure, but with increased bond dimensions.
- (ii) We continue adding columns, up to some $\ell = r$, where we start running out of resources. At that point, we have a tensor network with the MPS structure representing σ_L . Let us denote by $C_{\alpha,\beta}^n$ the basic tensor of that network, where $n = 1, \dots, D^2$ and $\alpha, \beta = 1, \dots, D^{2r}$ (n denotes the index at the (vertical) boundary, i.e., pointing in the horizontal direction).
- (iii) When the bond indices α, β grow larger than some predetermined value, say $D_c \leq D^{2r}$, we start approximating the tensor network using one with bond dimension D_c as follows. We first construct the tensor $K_{\alpha,\alpha';\beta,\beta'} = \sum_n C_{\alpha,\beta}^n \bar{C}_{\alpha',\beta'}^n$. Later we always deal with the case in which K is Hermitian (when considered as a matrix); if this is not the case, one can always choose a gauge where it is symmetric.¹³ We determine the eigenvector, $X_{\beta,\beta'}$, corresponding to the maximum eigenvalue of K , diagonalize X , consider the D_c largest eigenvalues, and build a projector onto the corresponding eigenspace. We then truncate the indices α and β by projecting onto that subspace.
- (iv) We continue in the same vein until the truncated tensor structure converges, which corresponds to the limit $N_h \rightarrow \infty$.
- (v) We can do the same with σ_R by going from right to left. For the examples studied below, $\sigma_L = \sigma_R =: \sigma_b = \sigma_b^T$, and thus we have to carry out this procedure just once.

IV. NUMERICAL RESULTS FOR AKLT MODELS

We now investigate some particular cases. We concentrate on the Affleck, Kennedy, Lieb, and Tasaki (AKLT) model,^{22–24} whose ground state, $|\Psi\rangle$, can be exactly described by a PEPS with bond dimension $D = 2$, as shown in Figs. 2 and 3. The spins in the first and last columns have $S = 3/2$, whereas the rest have $S = 2$. The AKLT Hamiltonian is given by a sum of projectors onto the subspace of maximum total spin across each nearest-neighbor pair of spins,

$$H_{\text{AKLT}} = \sum_{(n,m)} P_{n,m}^{(s)}, \quad (17)$$

where $P_{n,m}^{(s)}$ is the projector onto the symmetric subspace of spins n and m . This Hamiltonian is $su(2)$ and translationally invariant. This invariance is inherited by the virtual ancillas, and thus σ_b and H_b are also inherited. These symmetries can be used in the numerical procedures. Note that if H_b has these symmetries and has short-range interactions, then, since the ancillas have spin-1/2 (as $D = 2$), it is generically critical.

The lattice is bipartite. It is convenient to apply the operator $\exp(i\pi S_y/2)$ to every spin on the B sublattice: this unitary operator does not change the properties of ρ_ℓ but rather slightly simplifies the description of the PEPS. Thus, we can write the AKLT Hamiltonian as in Eq. (17) but with $P_{n,m}^{(s)} \rightarrow \tilde{P}_{n,m} := \exp(i\pi(f_n S_{y,n} + f_m S_{y,m})) P_{n,m}^{(s)} \exp(i\pi(f_n S_{y,n} + f_m S_{y,m}))$, with $f_n = 0, 1/2$ if the spin n is in the A or B sublattice, respectively.

We study finite N_h -leg ladders, as well as infinite square lattices. We start out in the next subsection with the simplest case of $N_h = 2$. Note that for this particular case the subsystem we consider when we trace one of the legs is a spin chain itself, so the density operator $\rho_{\ell=1}$ already describes

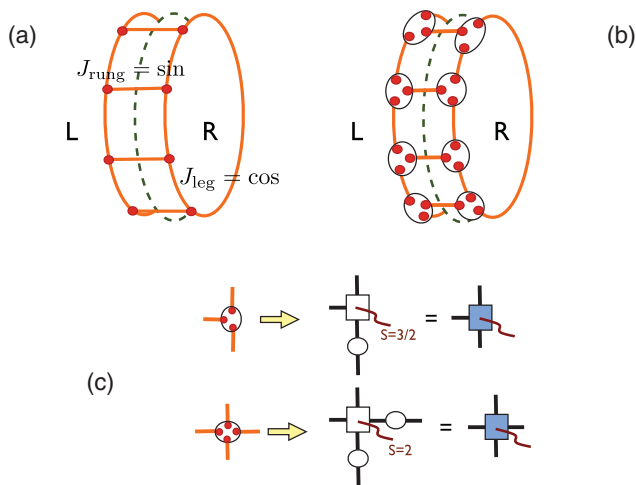


FIG. 2. (Color online) (a) Ribbon made of two ($N_h = 2$) coupled periodic $S = 1/2$ Heisenberg chains (two-leg ladder). (b) Ground state of a two-leg $S = 3/2$ AKLT ladder. Each site is split into three spins-1/2 (red dots). Nearest-neighbor spins-1/2 are paired up into singlet valence bonds. (c) PEPS representation for $S = 3/2$ and $S = 2$ sites of AKLT wave functions in the valence bond (singlet) picture (for connection to the “maximally entangled picture”; see text). Open squares indicate the $r_{\alpha_1, \alpha_2, \alpha_3}^m$ and $A_{\alpha_1, \alpha_2, \alpha_3, \alpha_4}^m$ tensors defined in the text and open circles correspond to the 2×2 matrix $[0, 1; -1, 0]$.

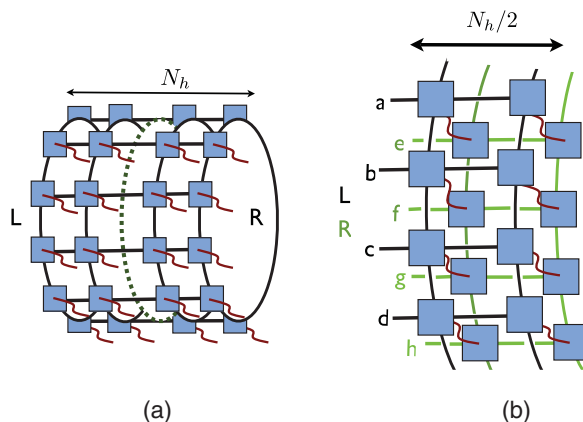


FIG. 3. (Color online) (a) Four-leg ($N_h = 4$) AKLT ladder on a cylinder partitioned (dotted green line) into two halves. (b) Schematic representation of the density matrix σ_b^2 of a four-leg ($N_h = 4, \ell = 2$) AKLT ladder. After being “cut” the two halves are “glued” together (physical indices are contracted).

a one-dimensional system and thus the physical spins already represent the boundary. In such a case, we do not need to resort to the PEPS formalism but we can also study other model Hamiltonians besides the AKLT one. For example, we consider the $su(2)$ -symmetric Heisenberg ladder Hamiltonian of $S = 1/2$ [Fig. 2(a)],

$$H_{\text{Heis}} = \sum_{(n,m)} J_{n,m} \mathbf{S}_n \cdot \mathbf{S}_m, \quad (18)$$

where the exchange couplings $J_{n,m}$ are parametrized by some angle θ ; i.e., $J_{\text{leg}} = \cos\theta$ ($J_{\text{rung}} = \sin\theta$) for nearest-neighbor sites n and m on the legs (rungs) of the ladder. Although the ground state has no simple PEPS representation, it can be obtained numerically by standard Lanczos exact diagonalization techniques on finite clusters of up to 14×2 sites.¹⁵ Similarly to the AKLT two-leg ladder [Fig. 2(b)], it possesses a finite magnetic correlation length ξ which diverges when $\theta \rightarrow 0$ (decoupled chain limit). The opposite limit $\theta = \pi/2$ ($\theta = -\pi/2$) corresponds to decoupled singlet (triplet) rungs (strictly speaking, with zero correlation length).

For infinite systems, we are also interested in the behavior of H_b along a quantum phase transition. To this aim, we also consider a distorted version of the AKLT model, and we define a family of Hamiltonians

$$H(\Delta) = \sum_{(n,m)} Q_n(\Delta) Q_m(\Delta) \tilde{P}_{n,m} Q_n(\Delta) Q_m(\Delta), \quad (19)$$

where $Q_n(\Delta) = e^{-4\Delta S_z^2}$. Note that the Hamiltonian is translationally invariant and has $u(1)$ symmetry. As Δ increases, it penalizes (nematic) states with $S_z = 0$, and thus the spins tend to take their maximum value of S_z^2 . As we show, there exists a critical value of Δ where a quantum phase transition occurs.

A. Two-leg ladders: Comparison between AKLT and Heisenberg models

Let us start out with the $su(2)$ -symmetric $\Delta = 0$ AKLT model in a two-leg ladder configuration, where ρ_ℓ corresponds to the state of one of the legs; that is, we take $N_h = 2$, $\ell = 1$, and all spins have $S = 3/2$ as shown in Fig. 2(b). The Hamiltonian is gapped,^{22,23} and the ground state is a PEPS with bond dimension $D = 2$. The tensors corresponding to the two legs, l and r , coincide and are given by $r_{\alpha_1, \alpha_2, \alpha_3}^m = \langle s_m | \alpha_1, \alpha_2, \alpha_3 \rangle$, where $\alpha_i = \pm 1/2$, and $|s_m\rangle$ is the state in the symmetric subspace of the three spin-1/2 with $S_z |s_m\rangle = m |s_m\rangle$, $m = -3/2, -1/2, 1/2, 3/2$.

We first examine the entanglement spectrum of H_b computed on a 16×2 ladder. It is shown in Fig. 4(b) as a function of the momentum along the legs, making use of translation symmetry (the vertical direction is periodic) enabling us to block-diagonalize the reduced density matrix in each momentum sector K . Note that it is also easy to implement the conservation of the z component S_z of the total spin so that each eigenstate can also be labeled according to its total spin S . The low-energy part of the spectrum clearly reveals zero-energy modes at $K = 0$ and $K = \pi$ consistent with the conformal field theory of central charge $c = 1$.

It is of interest to compare the two-leg AKLT results to the ones of the two-leg $S = 1/2$ Heisenberg ladder (18) sketched in Fig. 2(a) and investigated in Ref. 15. Figure 4(a), obtained on a 14×2 ladder for a typical parameter $\theta = \pi/3$, shows the entanglement spectrum of ρ_ℓ which, again, is very similar to that of a single nearest-neighbor Heisenberg chain. As mentioned in Ref. 15, in the first approximation, varying the parameter θ (and hence the ladder spin-correlation length) only changes the overall scale of the energy spectrum. Hence, it has been suggested¹⁵ to connect this characteristic energy scale to an effective inverse temperature β_{eff} .

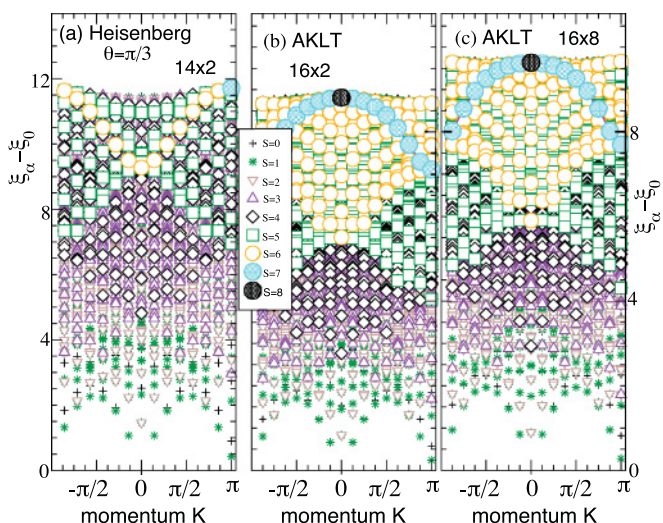


FIG. 4. (Color online) Entanglement spectra of H_b (with respect to the ground-state energy ξ_0) vs total momenta K in the chain (vertical) direction. (a) Two-leg (14×2) quantum Heisenberg ladder, (b) two-leg (16×2) AKLT ladder, and (c) eight-leg (16×8) AKLT ladder. The eigenvalues are labeled according to their total spin quantum number using different symbols (according to the legend on the graph).

The above results strongly suggest that H_b is “close” to a one-dimensional nearest-neighbor Heisenberg Hamiltonian. To refine this statement and make it more precise, we perform an expansion in terms of $su(2)$ -symmetric extended-range exchange interactions,

$$H_b = A_0 N_v + \sum_{r,k} A_r \mathbf{S}_k \cdot \mathbf{S}_{k+r} + R \hat{X}, \quad (20)$$

where $R \hat{X}$ stands for the “rest,” i.e., (small) multispin interactions. The amplitudes A_r can be computed from simple trace formulas,

$$A_r = \frac{4}{N_v} \text{tr} \left\{ H_b \sum_k \sigma_k^z \sigma_{k+r}^z \right\} / 2^{N_v}, \quad (21)$$

requiring the full knowledge of the eigenvectors of H_b (i.e., of σ_b). The value of A_0 is fixed by some normalization condition, e.g., $\text{tr} \sigma_b = 1$. Assuming \hat{X} is normalized as an extensive operator in N_v , i.e., $\frac{1}{N_v} \text{tr} \{ \hat{X}^2 \} = 2^{N_v}$, the amplitude R is given by

$$R^2 = \frac{1}{N_v} \text{tr} \{ H_b^2 \} / 2^{N_v} - N_v A_0^2 - \frac{3}{16} \sum_{r=1}^{N_v/2} A_r^2. \quad (22)$$

The coefficients A_r and R of two-leg Heisenberg ladders are plotted in Fig. 5(a) as a function of the parameter θ , in both the Haldane ($J_{\text{rung}} < 0$, i.e., ferromagnetic) and the rung singlet phases ($J_{\text{rung}} > 0$, i.e., antiferromagnetic). Generically, we find that H_b is *not frustrated*; i.e., all couplings at odd (even) distances are antiferromagnetic (ferromagnetic), $A_r > 0$ ($A_r < 0$). Clearly, the largest coupling is the nearest-neighbor one

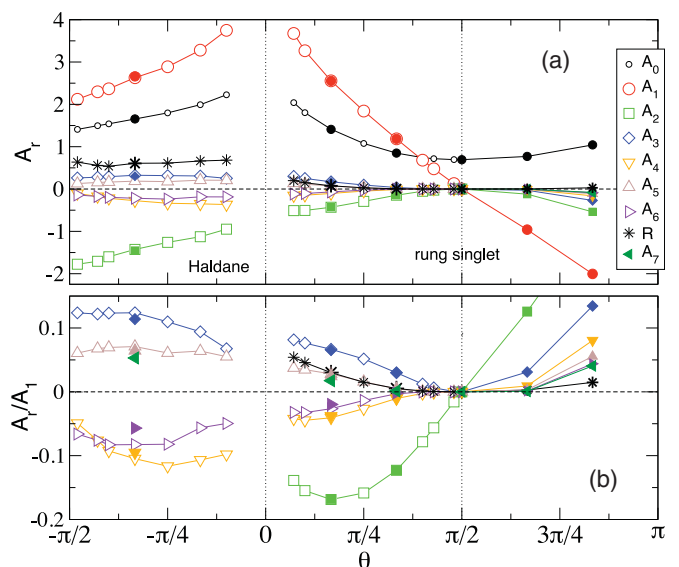


FIG. 5. (Color online) (a) Amplitudes A_r of the (isotropic) spin-spin couplings up to distance $r = 7$ of the effective boundary Hamiltonian of a quantum Heisenberg two-leg ladder in the Haldane and rung singlet phases vs θ . (b) Ratio of the same amplitudes normalized to the nearest-neighbor coupling ($r = 1$). Computations are carried out on 12×2 (open symbols) and 14×2 (closed symbols) systems. Note that when $\theta \rightarrow \pi/2$ (decoupled rung singlets), $A_r/A_0 \rightarrow 0$ for $r \geq 1$ and all the weights of the reduced density matrix become equal to 2^{-N_v} ($A_0 = \ln 2$).

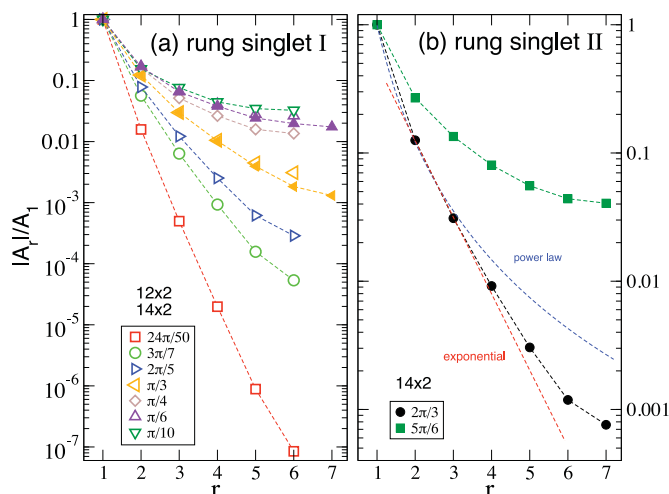


FIG. 6. (Color online) Two-leg quantum Heisenberg ladders: ratio of the amplitudes $|A_r|$ by the nearest-neighbor amplitude A_1 plotted using a logarithmic scale as a function of r for different values of θ . (a) Antiferromagnetic and (b) ferromagnetic leg couplings (the rung couplings are antiferromagnetic in both cases).

($r = 1$). Figure 5(b) shows the relative magnitudes of the couplings at distance $r > 1$ with respect to A_1 . These data suggest that the effective boundary Hamiltonian H_b is short range, especially in the strong rung coupling limit ($\theta \rightarrow \pi/2$) where $|A_{r'}/A_r| \rightarrow 0$ for $r' > r$. The amplitude A_1 of the nearest-neighbor interaction can be identified to the effective inverse temperature β_{eff} which, therefore, vanishes (diverges) in the strong (vanishing) rung coupling limit.

Next, we investigate the functional form of the decay of the amplitudes $|A_r|$ with distance. The ratio $|A_r|/A_1$ versus r is plotted (using semilog scales) in Figs. 6(a) and 6(b) for 12×2 and 14×2 Heisenberg ladders, respectively, with different values of θ . Similar data for a 20×2 AKLT ladder is shown in Fig. 7(a), providing clear evidence of *exponential* decay of the amplitudes with distance:

$$|A_r| \sim \exp(-r/\xi_b). \quad (23)$$

The Heisenberg ladder data are also consistent with such behavior (even though finite size corrections are stronger than for the AKLT case, especially when $\theta \rightarrow 0$ or π). It is not clear, however, how deep is the connection between the emerging length scale ξ_b and the two-leg ladder spin correlation length ξ . Note that the latter can be related¹⁵ to some effective *thermal* length associated to the inverse temperature $\beta_{\text{eff}} \propto A_1$.

Thanks to the PEPS representation of their ground state, AKLT ladders can be (exactly) handled up to larger sizes than their Heisenberg counterparts (typically up to $N_v = 20$), enabling a careful finite size scaling analysis of the boundary Hamiltonian (20). As shown in Fig. 8(a) for two-leg ($N_h = 2$) ladders, we observe a very fast exponential convergence of the coefficients A_r with the ladder length N_v ,

$$|A_r| = A_r^\infty + c_1 \exp\left(-\frac{N_v}{c_2}\right), \quad (24)$$

where c_1 and c_2 are two positive adjustable parameters. Hence, one gets at least seven (three) digits of accuracy for all distances up to $r = 5$ ($r = 7$) in the thermodynamic limit $N_h \rightarrow \infty$.

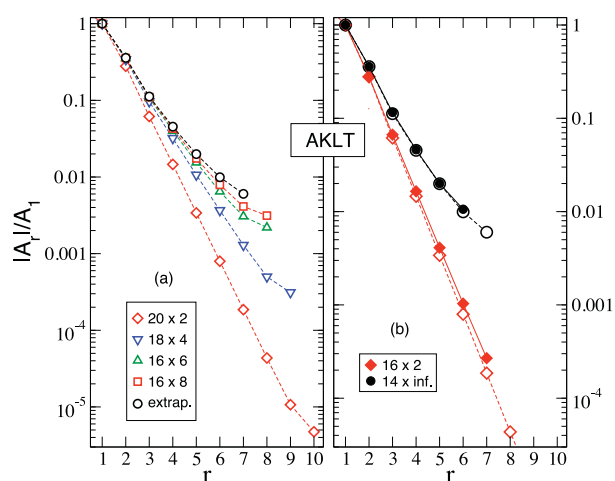


FIG. 7. (Color online) AKLT ladders: (a) Ratio $|A_r|/A_1$ plotted using a logarithmic scale as a function of r . Results are approximation free for finite N_h while the $N_h \rightarrow \infty$ limit is obtained by finite size scaling [see Fig. 8(b)]. (b) Comparison with $\sqrt{d_{r+1}/d_2}$ (solid symbols) computed (see text) on a two-leg and infinitely long ($N_h = \infty$) cylinder.

In fact, as pointed out previously, the boundary Hamiltonian H_b should not contain only two-body spin interactions. However, the total magnitude of all leftover (multibody) contributions, R , is remarkably small in the AKLT two-leg ladder; as shown in Fig. 8(a), $R < A_4$. In fact, the full magnitude of *all* many-body terms extending on $r + 1$ sites is given by $\sqrt{d_{r+1}}$ and can be compared directly to $|A_r|$ (after proper normalization). Figure 7(b) shows that $\sqrt{d_{r+1}/d_2}$ and $|A_r|/A_1$ are quite close, even at large distance. Note, however, that multibody interactions are significantly larger in the boundary Hamiltonian of the Heisenberg ladder, as shown

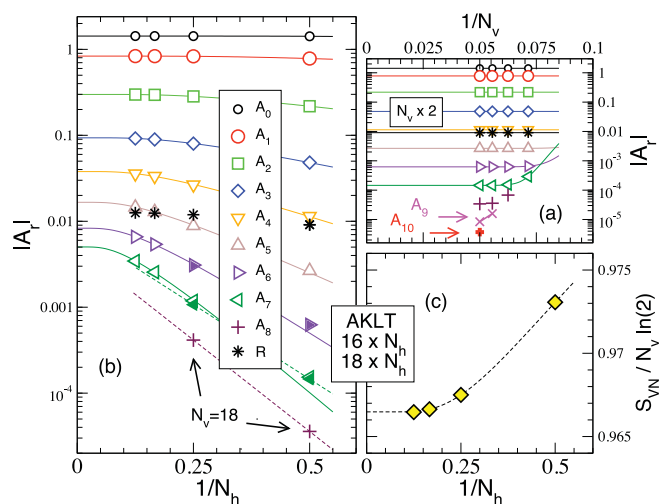


FIG. 8. (Color online) (a) Finite size scaling of the amplitudes A_r for a two-leg AKLT ladder vs $1/N_v$ ($N_v = 14, 16, 18, 20$). (b) Finite size scaling of the amplitudes A_r for N_h -leg AKLT ladders vs $1/N_h$ at fixed $N_v = 16$ (open symbols) or $N_v = 18$ (solid and + symbols). (c) Von Neumann (VN) entropy per unit length [normalized by $\ln(2)$] vs $1/N_h$ at fixed $N_v = 16$.

in Fig. 5 (although no accurate finite size scaling analysis can be done in that case).

B. N_h -leg AKLT ladder

Now we consider the AKLT model on an N_h -leg ladder configuration; we take $\ell = N_h/2$. The spins in the first and last legs have $S = 3/2$, and the corresponding tensors coincide with the ones given above. The rest of the spins have $S = 2$, and the corresponding tensor is $A_{\alpha_1, \alpha_2, \alpha_3, \alpha_4}^m = \langle s_m | \alpha_1, \alpha_2, \alpha_3, \alpha_4 \rangle$, where $\alpha_i = \pm 1/2$, and $|s_m\rangle$ is the state in the symmetric subspace of the four spin-1/2 with $S_z |s_m\rangle = m |s_m\rangle$, $m = -2, -1, 0, 1, 2$ [see Fig. 2(c)]. An example of a four-leg ladder and of a schematic representation of ρ_ℓ is shown in Fig. 3.

Let us now follow the same analysis (20) of the boundary Hamiltonian as we did for the case of two legs. The decay with distance of the coefficients A_r are reported in Fig. 7(a) for four-, six-, and eight-leg AKLT ladders. Clearly, the decay is still exponential with distance for all values of N_h studied but the characteristic length scale associated to this decay (directly given by the inverse of the slope of the curve in such a semilog plot) smoothly increases with N_h .

Next, we perform a careful finite size scaling analysis in Fig. 8(b) to extract the $N_h \rightarrow \infty$ limit of all A_r . We have access to cylinders of perimeter $N_v = 16$ ($N_v = 18$) with horizontal lengths $N_h = 2, 4, 6$, and 8 ($N_h = 2$ and 4) for which an exact contraction of the tensors can be done. Apart from the case when the distance r along the boundary approaches $N_v/2$, $A_r(N_h)$ depends very weakly on N_v and can be well fitted according to

$$\ln(|A_r|/A_r^\infty) = -\frac{c_3}{N_h} \exp\left(-\frac{N_h}{c_4}\right), \quad (25)$$

where c_3 and c_4 are two positive adjustable parameters. This extrapolation is very accurate up to $r = 5$, while reasonable estimates can still be obtained for $r = 6$ and $r = 7$. The extrapolated values of A_r^∞ are reported in Fig. 7(a), which shows that A_r also decays exponentially fast with r in an infinitely long cylinder ($N_h = \infty$). The characteristic emerging length scale is estimated to be still very short, around one lattice spacing.

Finally, we compute the von Neumann entanglement entropy defined by $S_{VN}[\sqrt{\rho_\ell}] = -\text{tr}\{\sqrt{\rho_\ell} \ln \sqrt{\rho_\ell}\}$ with the appropriate normalization $\text{tr}\{\sqrt{\rho_\ell}\} = 1$. S_{VN} scales like N_v (area law) and is bounded by $N_v \ln 2$. Figure 8(c) shows that the entropy converges very quickly with N_h to its thermodynamic value, which is very close to the maximum value. The entanglement of the two halves of the AKLT cylinder is therefore very strong. Note that very similar results are obtained using ρ_ℓ instead of $\sqrt{\rho_\ell}$.

C. Thermodynamic limit and phase transitions

Now we consider the $N_v, N_h \rightarrow \infty$ for the deformed AKLT model in order to investigate the phase transition. We compare some of the results with the two-leg ladder as well. The spins in the first and last legs have $S = 3/2$, and the rest have $S = 2$. The corresponding tensors are defined according to

$$\begin{aligned} l_{\alpha_1, \alpha_2, \alpha_3}^m &= r_{\alpha_1, \alpha_2, \alpha_3}^m = \langle s_m | Q(-\Delta) | \alpha_1, \alpha_2, \alpha_3 \rangle, \\ A_{\alpha_1, \alpha_2, \alpha_3, \alpha_4}^m &= \langle s_m | Q(-\Delta) | \alpha_1, \alpha_2, \alpha_3, \alpha_4 \rangle, \end{aligned} \quad (26)$$

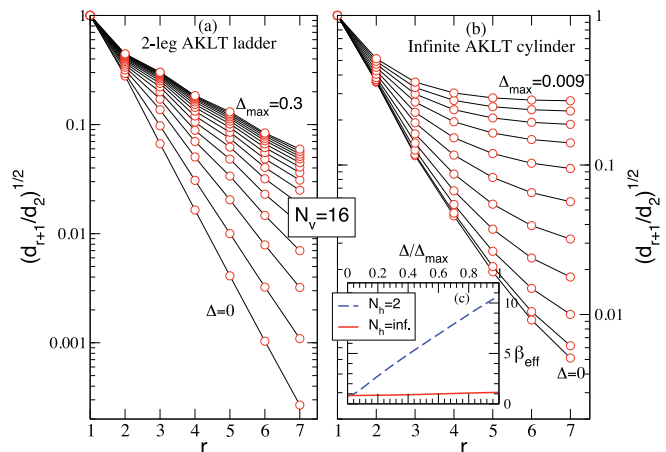


FIG. 9. (Color online) AKLT model with finite “nematic” field Δ : (a) Relative amplitude $\sqrt{d_{r+1}/d_2}$ in a two-leg ladder plotted using a logarithmic scale as a function of r and (b) the same for an infinitely long cylinder ($N_h = \infty$). From bottom to top, Δ is incremented from 0 to Δ_{\max} by constant steps. (c) Effective temperature β_{eff} [see Eq. (27)] vs Δ for the two cases reported in (a) and (b). All results are obtained for $N_v = 16$ ($D_c = 50$, and 100 iterations such that the tensors C already converge).

where $\alpha_i = \pm 1/2$, and $|s_m\rangle$ is the state in the symmetric subspace of the three (four) spin-1/2 with $S_z |s_m\rangle = m |s_m\rangle$, $m = -3/2, -1/2, 1/2, 3/2$ ($m = -2, -1, 0, 1, 2$), respectively.

We use the approximate procedure sketched in Sec. III C. In particular, for N_v larger than the correlation length, the obtained tensors $C_{\alpha, \beta}^n$ are independent of N_v . We have considered those tensors (with $D_c = 50$ and 100 iterations) and built σ_b and H_b out of them. Note that the $su(2)$ symmetry is explicitly broken by a finite Δ so that it becomes more convenient to use the variable d_n of Eq. (14) instead of A_r to probe the spatial extent of H_b . We recall that $(d_n)^{1/2}$ is the mean amplitude of *all* interactions acting at distance $r = n - 1$. We have plotted in Fig. 9 all d_n , $n \leq N_v/2$, for $N_v = 16$ as a function of Δ . As Δ increases, we see that the interaction length of the effective Hamiltonian increases and one sees a long-range interaction appearing. This indicates that we approach a phase transition. For the case of the ladder, the interaction length remains practically constant for the same range of variation of Δ .

Similarly to the investigation of the Heisenberg ladder,¹⁵ it is interesting to define an effective inverse temperature via the amplitude of the nearest-neighbor interaction,

$$\beta_{\text{eff}} = 8\sqrt{\frac{d_2}{3}}, \quad (27)$$

where the prefactor is introduced conveniently so that $\beta_{\text{eff}} = A_1$ in the $su(2)$ -symmetric limit $\Delta = 0$. As seen in the inset of Fig. 9, the inverse temperature of the ladder scales linearly with Δ . For the infinite cylinder, no singularity of β_{eff} is seen at the crossover between short- and long-range interactions.

Next, we plot the inverse correlation length as a function of Δ both for one dimension (i.e., an infinitely long ladder) and for two dimensions (i.e., $N_v = N_h = \infty$) in Fig. 10(a), obtained with $D_c = 150$ and 100 iterations. (No differences are observed by taking $D_c = 50$ and 50 iterations.) Clearly,

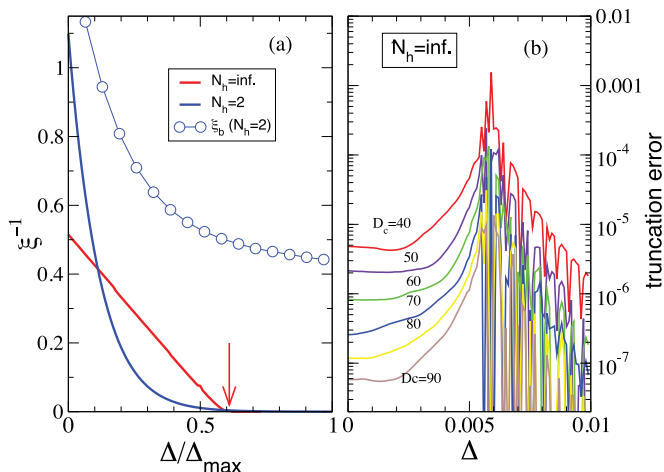


FIG. 10. (Color online) (a) Inverse correlation length ξ^{-1} vs Δ for both an AKLT two-leg ladder and an infinitely long cylinder ($N_h = \infty$). These data correspond to the infinite circumference limit, i.e., $N_v = \infty$. The arrow marks the phase transition in the infinitely long cylinder. Comparison with the inverse of the emerging length scale ξ_b is obtained by fitting the decay of the coefficients of H_b plotted in Fig. 9(a) as $\sqrt{d_{r+1}/d_2} \sim \exp(-r/\xi_b)$. (b) Truncation error in the $N_h \rightarrow \infty$ procedure. The results are compared with those obtained with $D_c = 150$, and 100 iterations have always been used.

the divergence of ξ (i.e., $\xi^{-1} = 0$) shows the appearance of a phase transition at $\Delta = 0.0061$ in two dimensions. In contrast, ξ^{-1} never crosses zero in the case of the ladder (i.e., in one dimension). We have compared ξ with the “emerging” length scale ξ_b obtained by fitting the decay of the coefficients of H_b as $\sqrt{d_{r+1}/d_2} \sim \exp(-r/\xi_b)$ on $N_v = 16$ two-leg and infinitely long (i.e., $N_h = \infty$) cylinders. In the two-leg ladder, we see that the divergence of the correlation length ξ for $\Delta \rightarrow \infty$ results from the interplay between (i) a (moderate) increase of the range ξ_b of the Hamiltonian H_b and (ii) a linear increase with Δ of the effective temperature scale β_{eff} , therefore approaching the $T_{\text{eff}} \rightarrow 0$ limit when $\Delta \rightarrow \infty$. This contrasts with the case of two dimensions ($N_v = N_h = \infty$) where the divergence of ξ occurs at *finite effective temperature* when H_b becomes sufficiently long range. However, it is hazardous to fit the decay of the coefficients of H_b to obtain its functional form at the phase transition. Finally, in Fig. 10(b) we have plotted the truncation error made by taking different D_c in the limit $N_h \rightarrow \infty$, and, again around $\Delta \approx 0.006$, the error increases. This is consistent with the expectation that, as H_b contains longer-range interaction, the boundary density operator σ_b requires a higher bond dimension to be described as a TN state.

V. NUMERICAL RESULTS FOR ISING PEPS

We now continue by considering the Ising PEPS introduced in Ref. 19. They all have bond dimension $D = 2$ and exhibit the \mathbb{Z}_2 symmetry of the transverse Ising chain. They depend on a single parameter, $\theta \in [0, \pi/4]$. For $\theta \sim \pi/4$ one has a state with all the spins pointing in the x direction, whereas for $\theta \sim 0$ the state is of Greenberger-Horne-Zeilinger (GHZ) type (a superposition of all spins up and all spins down). In the thermodynamic limit ($N_v, N_h \rightarrow \infty$) for $\theta \approx 0.35$ they

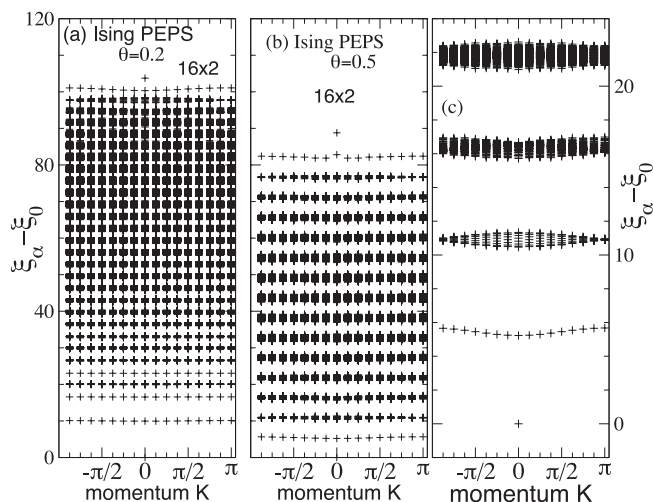


FIG. 11. Entanglement spectrum of a 16×2 Ising PEPS ladder vs momentum along the ladder leg direction. Comparison between (a) $\theta = 0.2$ and (b) $\theta = 0.5$ using the same energy scale. (c) Zoom in of the low-energy part of (b).

feature a phase transition, displaying critical behavior, where the correlation functions decay as a power law. Thus, by changing θ we can investigate how the boundary Hamiltonian behaves as one approaches the critical point.

A. Two-leg ladders

The tensors corresponding to the two legs, l and r , coincide and are given by $r_{\alpha_1, \alpha_2, \alpha_3}^m = a_m(\alpha_1)a_m(\alpha_2)a_m(\alpha_3)$, where $m = 0, 1$, $\alpha_i = \pm 1/2$, and $a_m(\alpha)$ are parametrized as $a_0(-1/2) = a_1(1/2) = \cos \theta$ and $a_0(1/2) = a_1(-1/2) = \sin \theta$.

As seen in Fig. 11, the entanglement spectrum of the two-leg ladder is gapped for all θ values and resembles that of an Ising chain (equally spaced levels) with small quantum fluctuations revealed by the small dispersion of the bands. The effective inverse temperature, qualitatively given by the gap (or the spacing between the bands), decreases for increasing θ .

The interaction length of the boundary Hamiltonian for the ladder is displayed in Fig. 12(a). The strength of the interactions decays exponentially with distance for all values of θ . As we increase this angle, one only observes a decrease of the interaction length. Note that, as opposed to the AKLT models studied in the previous sections, $d_1 \neq 0$. Indeed, there always exists a term with a single Pauli operator σ_x , describing an effective transverse field in H_b . Thus, that Hamiltonian is given by a transverse Ising chain in the noncritical region of parameters.

We have also plotted the inverse correlation length ξ^{-1} as a function of θ in Fig. 13 (open blue dots). Although the correlation length increases as θ decreases, it only tends to infinity in the limit $\theta \rightarrow 0$, as it must be for a GHZ state. No signature of a phase transition is found otherwise.

B. Thermodynamic limit and phase transitions

We now move to the case of an infinitely long cylinder. As above, to grow the cylinder in the horizontal direction, one considers rank 5 tensors, which here take the form

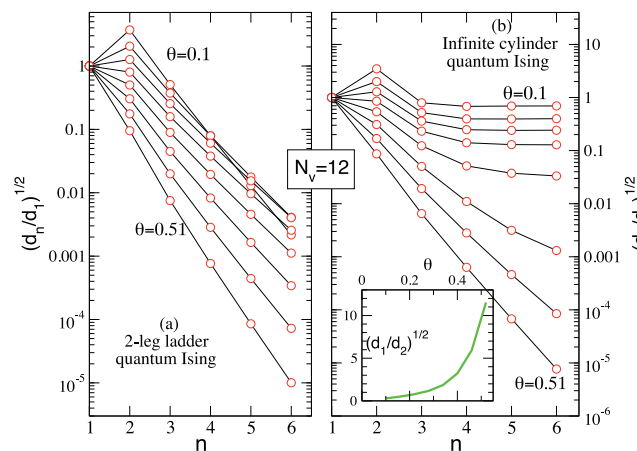


FIG. 12. (Color online) Ising PEPS: Relative amplitude $\sqrt{d_n/d_1}$ in (a) a two-leg ladder and (b) an infinitely long ($N_h = \infty$) cylinder as a function of n for θ varying from 0.1 to ~ 0.51 with constant intervals (0.1, 0.1585, 0.2171, 0.2756, 0.3342, 0.3927, 0.4512, and 0.5098, from top to bottom). Logarithmic scales are used on the vertical axis in both (a) and (b). Inset shows the ratio of the effective transverse field $\sqrt{d_1}$ over the effective Ising nearest-neighbor coupling $\sqrt{d_2}$ vs θ for $N_h = \infty$ ($D_c = 50$ and 100 iterations). All results are obtained for $N_v = 12$.

$A_{\alpha_1, \alpha_2, \alpha_3, \alpha_4}^m = a_m(\alpha_1)a_m(\alpha_2)a_m(\alpha_3)a_m(\alpha_4)$, using the same approximation scheme with 100 iterations as before.

The parameters d_n describing the boundary Hamiltonian H_b behave very differently in the ladder and infinite cylinders as shown in Fig. 12. While for the Ising PEPS ladder H_b remains short ranged with exponential decay of d_n versus n , the infinite cylinder shows a transition toward long-range interactions, suggesting the existence of a phase transition. This is very similar to what occurred in the AKLT distorted model.

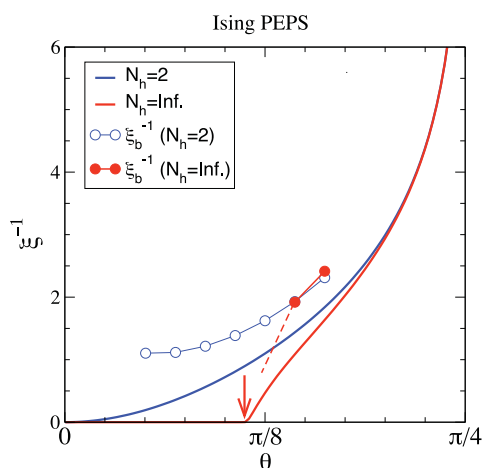


FIG. 13. (Color online) Ising PEPS: Inverse correlation length ξ^{-1} vs Δ for both two-leg ladder and infinitely long cylinder ($N_h = \infty$, $D_c = 150$ and 100 iterations). These data correspond to the infinite circumference limit, i.e., $N_v = \infty$. The arrow marks the phase transition in the infinitely long cylinder. Comparison with the inverse of the emerging length scale ξ_b^{-1} obtained by fitting the decay of the coefficients plotted in Fig. 12 as $\sqrt{d_n} \sim \exp(-n/\xi_b)$.

As long as H_b remains short range, the density matrix ρ_ℓ can be (qualitatively) mapped onto the thermal density matrix of an effective quantum Ising chain (including a “family” of transverse-like fields) and, therefore, no ordering is expected (at finite effective temperature). However, a phase transition can appear when H_b becomes long ranged as in the case for an infinitely long cylinder. This is evidenced by the behavior of correlation lengths computed for the two-leg and infinitely long ($N_h = \infty$) cylinder and reported in Fig. 13. These correlation lengths are compared to the respective emerging length scales ξ_b characterizing the decay of $\sqrt{d_n}$ with n . In the two-leg ladder case, ξ_b increases quite moderately when $\theta \rightarrow 0$ ($\xi_b \sim 1$), so the divergence of the correlation length ξ in this limit is only attributed to a *vanishing* of the effective temperature scale T_{eff} . In contrast, as for the AKLT model, the phase transition in two dimensions occurs at finite (effective) temperature at the point where $\xi_b \rightarrow \infty$.

In summary, these results evidence that, whenever we approach a phase transition, the interaction length of the boundary Hamiltonian increases.

VI. TOPOLOGICAL KITAEV CODE

Let us finally consider systems with topological order. We focus on Kitaev’s code state:²⁵ It can be defined on a square lattice with spin-1/2 systems (qubits) on the vertices, with two types of terms in the Hamiltonian,

$$h_X = X^{\otimes 4}, \quad h_Z = Z^{\otimes 4} \quad (28)$$

(where X and Z are Pauli matrices), each of which acts on the four spins adjacent to a plaquette, and where the h_X and h_Z form a checkerboard pattern [see Fig. 14(a)]. The ground-state subspace of the code state can be represented by a PEPS with $D = 2$ ¹⁹; a particularly convenient representation is obtained by taking 2×2 blocks of spins across h_Z -type plaquettes and jointly describing the spins in each block by one tensor of the form²⁶

$$A_{\alpha_1, \alpha_2, \alpha_3, \alpha_4}^{i_{1,2}, i_{2,3}, i_{3,4}, i_{4,1}} = \begin{cases} 1 & \text{if } i_{x,x+1} = \alpha_{x+1} - \alpha_x \pmod{2} \forall x, \\ 0 & \text{otherwise.} \end{cases} \quad (29)$$

Here, $i_{x,x+1}$ denotes the spin located between the bonds α_x and α_{x+1} (numbered clockwise), as shown in Fig. 14(b). It can be checked straightforwardly that the resulting tensor network is an eigenstate of the Hamiltonians of Eq. (28). Excitations of the model correspond to violations of h_X terms (charges) or h_Z terms (fluxes), which always come in pairs.²⁵

We put the code state on a cylinder of $N_h \times N_v$ tensors (i.e., $2N_h \times 2N_v$ sites), where we choose boundary conditions

$$|\chi_\theta\rangle = \cos \frac{\theta}{2} |0\rangle^{\otimes N_v} + \sin \frac{\theta}{2} |1\rangle^{\otimes N_v}. \quad (30)$$

This yields a state which is also a ground state of $h_Z^b = Z^{\otimes 2}$ terms at the boundary, but not of the corresponding $X^{\otimes 2}$ boundary terms; in other words, charges (Pauli Z errors) can condense at the boundaries of the cylinder.²⁷ The full Hamiltonian—including the h_Z^b terms at the boundary—has a twofold degenerate ground state which is topologically protected, and where the logical X and Z operators are a loop of Pauli X ’s around the cylinder and a string of Pauli Z ’s between its two ends (where they condense), respectively.

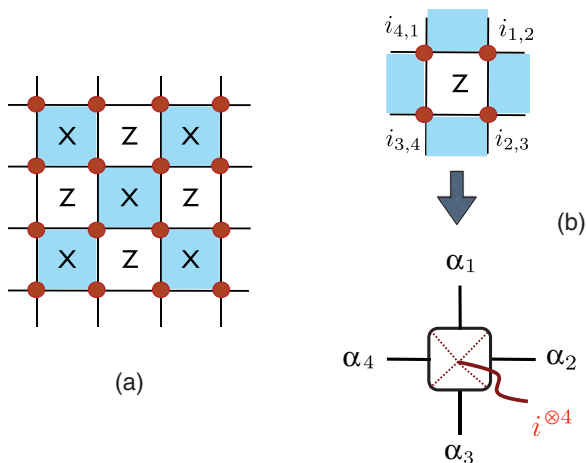


FIG. 14. (Color online) (a) Checkerboard decomposition in the Kitaev code. Spin-1/2 are represented by (red) dots at the vertices of the square lattice. X and Z operators act on the four spins of each type of (shaded and nonshaded) plaquettes. (b) PEPS representation of the Kitaev code (see text).

To compute ρ_ℓ , we start by considering the PEPS on the cylinder without boundary conditions (30), i.e., with open virtual indices at both ends (labeled B and B'). Cutting the cylinder in the middle leaves us with σ_{BL} , the joint reduced density operator for the virtual spaces at the boundary, B (or B'), and the cut, L (or R). From Eq. (29), one can readily infer that the transfer operator for a single tensor is $\mathbb{1}^{\otimes 4} + X^{\otimes 4}$ and, thus,

$$\sigma_{BL} = \sigma_{B'R} \propto \mathbb{1}^{\otimes N_v} \otimes \mathbb{1}^{\otimes N_v} + X^{\otimes N_v} \otimes X^{\otimes N_v}, \quad (31)$$

where the two tensor factors correspond to the B (B') and L (R) boundary, respectively. Imposing the boundary condition $|\chi_\theta\rangle\langle\chi_\theta|$, Eq. (30), at B (B'), we find that (up to normalization)

$$\rho_\ell \propto (1 + \sin^2 \theta) \mathbb{1}^{\otimes N_v} + (2 \sin \theta) X^{\otimes N_v},$$

which is the thermal state $\rho_\ell \propto \exp[-\beta_{\text{eff}} H_\ell]$ of $H_\ell = -\text{sign}(\sin \theta) X^{\otimes N_v}$ at an effective inverse temperature

$$\beta_{\text{eff}} = \left| \tanh^{-1} \left[\frac{2 \sin \theta}{1 + \sin^2 \theta} \right] \right|.$$

The fact that H_ℓ acts globally is a signature of the topological order, and it comes from the fact that measuring an X loop operator gives a nontrivial outcome (namely $\sin \theta$). Note that the entropy $S(\rho_\ell)$ increases by one as $1/\beta_{\text{eff}}$ goes from zero to infinity. This can be understood as creating an entangled pair of charges $|\text{vac}\rangle + f(\beta_{\text{eff}})|c, c^*\rangle$ across the cut, thereby additionally entangling the two sides by at most an ebit and subsequently condensing the charges at the boundaries.

Instead of considering σ_L , one can also see the topological order by looking at σ_{BL} : It is the zero-temperature state of a completely nonlocal Hamiltonian $X^{\otimes N_v} \otimes X^{\otimes N_v}$ which acts simultaneously on both boundaries in a maximally nonlocal way; this relates to the fact that the expectation values of any two X loop operators around the cylinder are correlated.

Let us point out that systems with conventional long-range order behave quite differently, even though they also exhibit

correlations between distant boundaries. Consider the spin-1/2 Ising model without field, which has a PEPS tensor

$$A_{\alpha_1, \alpha_2, \alpha_3, \alpha_4}^i = \delta_{i, \alpha_1} \delta_{\alpha_1, \alpha_2} \delta_{\alpha_2, \alpha_3} \delta_{\alpha_3, \alpha_4}.$$

The resulting local transfer operator is $|0\rangle\langle 0|^{\otimes 4} + |1\rangle\langle 1|^{\otimes 4}$ and, thus,

$$\sigma_{BL} = |0\rangle\langle 0|^{\otimes N_v} + |1\rangle\langle 1|^{\otimes N_v}.$$

By imposing boundary conditions at B , one arrives at

$$\rho_\ell = \sin \theta |0\rangle\langle 0|^{\otimes N_v} + \cos \theta |1\rangle\langle 1|^{\otimes N_v},$$

which is the thermal state of the classical Ising Hamiltonian

$$H(\beta) = - \sum_i Z_i Z_{i+1} - \frac{\log \tan \theta}{2\beta N_v} \sum_i Z_i$$

for $\beta \rightarrow \infty$. Thus, for the Ising model, ρ_ℓ is described by a local Ising Hamiltonian rather than by a completely nonlocal interaction as for Kitaev's code state. The same holds true for σ_{BL} , which is the ground state of a classical Ising model without field: while it has correlations between the two boundaries, they arise from a local (i.e., few-body) interaction coupling the two boundaries rather than from terms acting on *all* sites on both boundaries together. Correspondingly, the long-range correlations in the Ising model can be already detected by measuring local observables instead of topologically nontrivial loop operators as for Kitaev's code state.

VII. CONCLUSIONS AND OUTLOOK

In this paper, we have introduced a framework which allows us to associate the bulk of a system with its boundary in the spirit of the holographic principle. To this end, we have employed the framework of PEPS, which provides a natural mapping between the bulk and the boundary, where the latter is given by the virtual degrees of freedom of the PEPS. This framework allows us to map the state of any region to a Hamiltonian on its boundary in such a way that the properties of the bulk system, such as the entanglement spectrum or the correlation length, are reflected in the properties of the Hamiltonian. Since our framework also identifies observables in the bulk with observables on the boundary, it establishes a general holographic principle for quantum lattice systems based on PEPS.

In order to elucidate the connection between the bulk system and the boundary Hamiltonian, we have numerically studied the AKLT model and the Ising PEPS. We found that the Hamiltonian is local for systems in a gapped phase with local order, whereas a diverging interaction length of the Hamiltonian is observed when the system approaches a phase transition, and topological order is reflected in a Hamiltonian with fully nonlocal interactions; thus, the quantum phase of the bulk can be read off the properties of the boundary model.

Our holographic mapping between the bulk and the boundary in the PEPS formalism has further implications. In particular, the contraction of PEPS in numerical simulations requires that the boundary operator be approximated by one with a smaller bond dimension, which can be done efficiently if the boundary describes the thermal state of

a local Hamiltonian, i.e., for noncritical systems. Also, since renormalization in the PEPS formalism requires that we discard the degrees of freedom in the bond space with the least weight,²⁸ the duality allows us to understand real-space renormalization in the bulk as Hamiltonian renormalization on the boundary.

Our techniques can also be applied to systems in higher dimensions, and in fact to arbitrary graphs, to relate the boundary of a system with its bulk properties. The mapping applies to arbitrary regions in the lattice, such as simply connected (e.g., square) regions used, for instance, for the computation of topological entropies. Also, relating the bulk to the boundary using the PEPS description can be generalized beyond spin systems by considering fermionic or anyonic PEPS,²⁹ as well as continuous PEPS in the case of field theories.^{30,31} Finally, when studying edge modes, the one-dimensional system which describes the physical boundary is given by a matrix product operator acting on the virtual boundary state and, thus, the relation between bulk properties

and the virtual boundary implies a relation between the properties of the bulk and its edge mode physics.

ACKNOWLEDGMENTS

We acknowledge the hospitality of the Kavli Institute for Theoretical Physics (University of California, Santa Barbara) where this work was initiated. DP acknowledges support by the French Research Council (Agence Nationale de la Recherche) under Grant No. ANR 2010 BLANC 0406-01 and thanks IDRIS (Orsay, France) and CALMIP (Toulouse, France) for the use of NEC-SX8 and Altix SGI supercomputers, respectively. NS acknowledges support by the Gordon and Betty Moore Foundation through Caltech's Center for the Physics of Information, NSF Grant No. PHY-0803371, and ARO Grant No. W911NF-09-1-0442. FV acknowledges funding from the SFB projects Vicom and Foqus and the EC projects QUERG and Quevadis. JIC acknowledges the EC project Quevadis, the DFG Forschergruppe 635, and Caixa Manresa.

¹M. Srednicki, *Phys. Rev. Lett.* **71**, 666 (1993).

²C. Holzhey, F. Larsen, and F. Wilczek, *Nucl. Phys. B* **44**, 424 (1994).

³M. B. Hastings, *J. Stat. Mech.* (2007) P08024.

⁴M. M. Wolf, F. Verstraete, M. B. Hastings, and J. I. Cirac, *Phys. Rev. Lett.* **100**, 070502 (2008).

⁵P. Calabrese and J. Cardy, *J. Stat. Mech.* (2004) P06002; e-print [arXiv:hep-th/0405152](https://arxiv.org/abs/hep-th/0405152).

⁶G. Vidal, J. I. Latorre, E. Rico, and A. Kitaev, *Phys. Rev. Lett.* **90**, 227902 (2003).

⁷S. R. White, *Phys. Rev. Lett.* **69**, 2863 (1992).

⁸U. Schollwöck, *Rev. Mod. Phys.* **77**, 259 (2005).

⁹F. Verstraete, V. Murg, and J. I. Cirac, *Adv. Phys.* **57**, 143 (2008).

¹⁰J. I. Cirac and F. Verstraete, *J. Phys. A: Math. Theor.* **42**, 504004 (2009).

¹¹F. Verstraete and J. I. Cirac, *Phys. Rev. B* **73**, 094423 (2006).

¹²M. Fannes, B. Nachtergaele, and R. F. Werner, *Commun. Math. Phys.* **144**, 443 (1992).

¹³D. Perez-Garcia, F. Verstraete, M. M. Wolf, and J. I. Cirac, *Quantum Inf. Comput.* **7**, 401 (2007).

¹⁴H. Li and F. D. M. Haldane, *Phys. Rev. Lett.* **101**, 010504 (2008).

¹⁵D. Poilblanc, *Phys. Rev. Lett.* **105**, 077202 (2010).

¹⁶F. Verstraete and J. I. Cirac, e-print [arXiv:cond-mat/0407066](https://arxiv.org/abs/cond-mat/0407066).

¹⁷F. Verstraete and J. I. Cirac, *Phys. Rev. A* **70**, 060302 (2004).

¹⁸M. B. Hastings, *Phys. Rev. B* **76**, 035114 (2007).

¹⁹F. Verstraete, M. M. Wolf, D. Perez-Garcia, and J. I. Cirac, *Phys. Rev. Lett.* **96**, 220601 (2006).

²⁰I. Peschel, M. Kaulke, and O. Legeza, *Ann. Phys.* **8**, 153 (1999).

²¹G. Vidal, *Phys. Rev. Lett.* **98**, 070201 (2007).

²²I. Affleck, T. Kennedy, E. H. Lieb, and H. Tasaki, *Phys. Rev. Lett.* **59**, 799 (1987).

²³I. Affleck, T. Kennedy, E. H. Lieb, and H. Tasaki, *Commun. Math. Phys.* **115**, 477 (1988).

²⁴For the computation of entanglement entropy of AKLT ladders, see H. Katsura, N. Kawashima, A. N. Kirillov, V. E. Korepin, and S. Tanaka, *J. Phys. A: Math. Theor.* **43**, 255303 (2010).

²⁵A. Kitaev, *Ann. Phys.* **303**, 2 (2003).

²⁶N. Schuch, J. I. Cirac, and D. Pérez-García, *Ann. Phys.* **325**, 2153 (2010).

²⁷E. Dennis, A. Kitaev, A. Landahl, and J. Preskill, *J. Math. Phys.* **43**, 4452 (2002).

²⁸Z. C. Gu, M. Levin, and X. G. Wen, *Phys. Rev. B* **78**, 205116 (2008).

²⁹C. V. Kraus, N. Schuch, F. Verstraete, and J. I. Cirac, *Phys. Rev. A* **81**, 052338 (2010).

³⁰F. Verstraete and J. I. Cirac, *Phys. Rev. Lett.* **104**, 190405 (2010).

³¹T. J. Osborne, J. Eisert, and F. Verstraete, *Phys. Rev. Lett.* **105**, 260401 (2010).